

Jamming is a first-order transition with quenched disorder in amorphous materials sheared by cyclic quasistatic deformations

Received: 11 March 2024

Yue Deng^{1,2}, Deng Pan¹ & Yuliang Jin^{1,2,3} ✉

Accepted: 1 August 2024

Published online: 16 August 2024

 Check for updates

Jamming is an athermal transition between flowing and rigid states in amorphous systems such as granular matter, colloidal suspensions, complex fluids and cells. The jamming transition seems to display mixed aspects of a first-order transition, evidenced by a discontinuity in the coordination number, and a second-order transition, indicated by power-law scalings and diverging lengths. Here we demonstrate that jamming is a first-order transition with quenched disorder in cyclically sheared systems with quasistatic deformations, in two and three dimensions. Based on scaling analyses, we show that fluctuations of the jamming density in finite-sized systems have important consequences on the finite-size effects of various quantities, resulting in a square relationship between disconnected and connected susceptibilities, a key signature of the first-order transition with quenched disorder. This study puts the jamming transition into the category of a broad class of transitions in disordered systems where sample-to-sample fluctuations dominate over thermal fluctuations, suggesting that the nature and behavior of the jamming transition might be better understood within the developed theoretical framework of the athermally driven random-field Ising model.

Jamming in athermal particles is a paradigm of transitions between fluids and amorphous solids^{1–5}, with a deep connection to the glass transition in thermal systems^{6–8}. Recent studies have revealed extremely rich features in the jamming phenomenon, but the nature of the jamming transition remains inconclusive.

(i) *Mechanical marginality, related diverging length scales, and power-law scalings.* At the jamming transition density (volume fraction) φ_j , the isostatic condition needs to be satisfied for the coordination number Z (average number of contacts per particle): $Z = Z_{\text{iso}} = 2d$ in frictionless, infinite systems, where d is the dimensionality^{9,10}. Isostaticity implies that at φ_j the system is marginally stable, inspiring the search for diverging length scales. According to the “cutting argument”, the isostaticity gives rise to a diverging isostatic length scale at jamming,

$l^* \sim \Delta Z^{-1} \sim (\varphi - \varphi_j)^{-1/2}$, below which mechanical stability of the bulk system is affected by the cutting boundaries^{11–13}, where $\Delta Z = Z - Z_{\text{iso}}$ is the excess coordination number. The effective medium theory gives a scattering length scale diverging at φ_j , $l_c \sim \Delta Z^{-1/2} \sim (\varphi - \varphi_j)^{-1/4}$, below which continuum elasticity breaks down^{14–16}. Other related diverging length scales include the transverse wavelength, $\xi_T \sim (\varphi - \varphi_j)^{-\nu_T}$ with $\nu_T \approx 0.24$ ¹³, and the longitudinal wavelength, $\xi_L \sim (\varphi - \varphi_j)^{-\nu_L}$ with $\nu_L \approx 0.48$ ¹³.

At jamming, the marginal stability analysis provides relationships between the exponents θ appearing in the power-law distribution of weak inter-particle forces $P(f) \sim f^{-\theta}$ and α in the distribution of small inter-particle gaps $P(h) \sim h^{-\alpha}$: $\theta = 1/\alpha - 2$ for extensive modes¹⁷ and $\theta = 1 - 2\alpha$ for localized buckling modes^{18,19}. Above jamming, the marginal boundary between unstable and stable phases is defined by a scaling relation, $\Delta Z \sim (\varphi - \varphi_j)^{1/2}$ ^{21,20}.

¹Institute of Theoretical Physics, Chinese Academy of Sciences, Beijing 100190, China. ²School of Physical Sciences, University of Chinese Academy of Sciences, Beijing 100049, China. ³Center for Theoretical Interdisciplinary Sciences, Wenzhou Institute, University of Chinese Academy of Sciences, Wenzhou, Zhejiang 325001, China. ✉e-mail: yuliangjin@mail.itp.ac.cn

- Other scalings have been established for over-jammed systems near $\varphi_j^{1-3,5,21,22}$. For example, a relationship between the shear modulus G and ΔZ can be derived by microscopic elastic theories, $G \sim \Delta Z \sim (\varphi - \varphi_j)^{1/2,11,23,24}$.
- (ii) **Hyperuniformity and associated diverging length scales.** Recent studies reveal that the spatial distribution of the single-particle contact number, Z_i , is hyperuniform at jamming. The contact hyperuniformity is established by two power-law scalings measured in simulated packings^{25,26}: the scaling of the fluctuations of the average contact number in a hyper-cube of volume ℓ^d , $\sigma_Z(\ell) \sim \ell^{-\mu}$ with $\mu = 1$, and the small wave-vector scaling of the contact number structure factor, $S_Z(q) \sim q^{-\alpha_Z}$ with $\alpha_Z \approx 1.53$. The crossover from the hyperuniform regime ($\ell \ll \xi_H$) to the uniform regime ($\ell \gg \xi_H$) defines a hyperuniform correlation length ξ_H , which diverges at the jamming transition, $\xi_H \sim \Delta Z^{-1/4}$. The value of the exponent ν_H appears to depend on how to extract the correlation length and the dimensionality.
- (iii) **Gardner glass phase, landscape marginality and associated criticality.** The marginality at jamming has been established by an independent approach within the framework of replica symmetry breaking^{8,27-32}. Unjammed hard-sphere glasses undergo a Gardner transition where the free energy landscape becomes fractal and marginal, and the caging susceptibility diverges²⁹. The entire Gardner phase, including the jamming limit, is critical. In other words, the caging correlation length, $\xi_G \sim \infty$, remains infinite near jamming, when the transition is approached ($\varphi \rightarrow \varphi_j$) from below ($\varphi < \varphi_j$). The mean-field replica theory predicts the values of exponents in the weak force and small gap distributions, $\alpha = 0.41\dots$ and $\theta = 0.42\dots$, coinciding with the relationship $\theta = 1/\alpha - 2$ given by the mechanical marginal stability analysis^{27,33,34}. The theory provides an additional scaling relationship between the cage size Δ and the entropic pressure p , $\Delta \sim p^{-\kappa}$ with $\kappa = 1.41\dots$. The exponents appear to be independent of the dimensionality d for $d \geq d_u^{27,33,35}$, where $d_u = 2$ is the conjectured upper critical dimension of the jamming transition³⁶.
- (iv) **Criticality in shear rheology.** The criticality of the jamming transition is suggested by scaling analyses of the rheological data obtained in finite-rate shear simulations of flowing states near φ_j^{37-39} . Combining the power-law divergence of the viscosity, $\eta = (\varphi_j - \varphi)^{-\beta}$ and the vanishing of yield stress, $\sigma_Y \sim (\varphi - \varphi_j)^\Delta$, a critical scaling function is proposed. A diverging rheological correlation length can be extracted from velocity correlations³⁷ or non-affine displacements⁴⁰, $\xi_R \sim (\varphi_j - \varphi)^{-\nu}$, with $\nu \approx 1^{37,41,42}$. The criticality seems to be at odds with the hyperuniformity discussed in (ii) – in the thermodynamical limit, the fluctuations diverge in the former and vanish in the latter.
- (v) **Discontinuity in the coordination number.** The coordination number Z , which is considered as an order parameter of the jamming transition³, jumps discontinuously from $Z = 0$ below jamming, to $Z \geq Z_{iso}$ above, under quasistatic compression/decompression^{1,2} or shear⁴³. In unjammed states, $Z = 0$ because particles can push each other apart, leaving no overlapping between them. In jammed states, the contact network spans the entire system and the minimum condition to have such networks is $Z = Z_{iso}$. Thus the discontinuous jump in Z at jamming is essentially related to isostaticity. Apparently, as the signature of a first-order transition, this discontinuity is inconsistent with the viewpoint of a continuous transition described above. Note that not all physical quantities exhibit a discontinuity at jamming: some quantities, such as the pressure P and the shear modulus G , vanish continuously when the jamming transition is approached from above^{1,2} (for example, see ref. 44) for the relation between P and φ). On the other hand, other quantities, such as the bulk modulus B and the fraction of non-rattlers f_{NR} , jump abruptly at jamming, similar to Z .
- It is clear that various diverging length scales have been suggested throughout the literature. However, none of the lengths in (i–iv) can explain the finite-size scaling behavior of the jamming fraction $F_j(\varphi, N)^{2,45-47}$: the data can be reasonably collapsed by a scaling form, $F_j(\varphi, N) = \mathcal{F}[(\varphi - \varphi_j)N^{1/2}]$, valid for both compression and shear jamming in two (2D) and three (3D) dimensions. In this study, we show that this scaling can be fully explained by a first-order transition scenario of the jamming transition with quenched disorder. The form $(\varphi - \varphi_j)N^{1/2}$ originates from the disorder-induced fluctuation of the jamming density itself in finite-sized systems of N particles, which follows the standard central limit theorem. Thus this finite-size scaling is independent of isostaticity, marginality, criticality and hyperuniformity.
- Three important differences between previous approaches (i–v) and ours shall be denoted. First, in (i–iii), the jamming limit is approached from one side only, i.e., the over-jammed side ($\varphi > \varphi_j$) in (i) and (ii), and the unjammed side ($\varphi < \varphi_j$) in (iii). Here we consider a well-defined ensemble including both over-jammed and unjammed states, whose ratio is essential in the scaling analysis. Note that once an ensemble average is taken, the (v) discontinuity in Z turns into a smooth function, and thus a finite-size analysis becomes essential to see the asymptotic behavior in the thermodynamic limit.
- Second, in conventional compression protocols, the generated ensemble depends on the initial conditions⁴⁷⁻⁴⁹ and the basins of attraction^{45,50,51}. Here we instead consider an ensemble prepared by cyclic shear, where the states are sampled by well-controlled dynamics similar to those in thermal systems. Recently, the response of amorphous assemblies of particles to cyclic shear has attracted great interest, due to the presence of a non-equilibrium phase transition, called the reversible-irreversible (RI) transition⁵²⁻⁵⁶. Interestingly, the jamming transition lies in the irreversible regime where particle trajectories are asymptotically diffusive^{55,56}. In this study, we restrict our ensemble within the irreversible phase. The jamming density of this ensemble is equivalent to the minimum jamming density, or the jamming-point (J-point) density that is obtained by rapid quench². The protocol dependence of the jamming density is not observed in our simulations: the preparation history of the initial condition becomes irrelevant after the first shear cycle, because a steady state is reached before the strain reversal.
- Third, in our ensemble, we carefully exclude partially crystallized and fragile states with $Z < Z_{iso}$ that are sensitive to mechanical perturbations or protocol parameters, and regard them as unjammed states with $Z = 0$. Any transient and intermediate states generated during shear, which appear before the steady states, are excluded in our analysis. If such states are included, the discontinuity in Z diminishes and the jamming transition looks continuous, similar to the results reported in ref. 40 obtained by uniform shear. Thus we expect the impactibility between the criticality viewpoint in (iv) and our first-order picture originating from finite-rate effects. For finite-time scales, the existence of transient states with $Z < Z_{iso}$ can lead to a continuous jamming transition^{37,38,40}. However, our results suggest that, after a sufficiently long time, any configurations with $Z < Z_{iso}$ would eventually relax to unjammed states with zero energy and inter-particle contacts. Note that the timescale for the system to attain force balance diverges at the shear jamming transition⁴³, which means that the real quasistatic limit would correspond to extremely small shear rates in large systems.

Results

An ensemble generated by cyclic athermal quasistatic shear

We apply cyclic athermal quasistatic shear (CAQS) to standard models of soft, frictionless particles in 2D and 3D (see *Models* and *Shear protocol* in Methods). We present 2D data in the main text and 3D data in the Supplementary Information (SI). For the 2D model, previous studies report a jamming density (J-point density) $\varphi_j \approx 0.842 - 0.843^{41,57}$. The phase diagram of RI transitions near φ_j is plotted in Fig. 1a. The RI

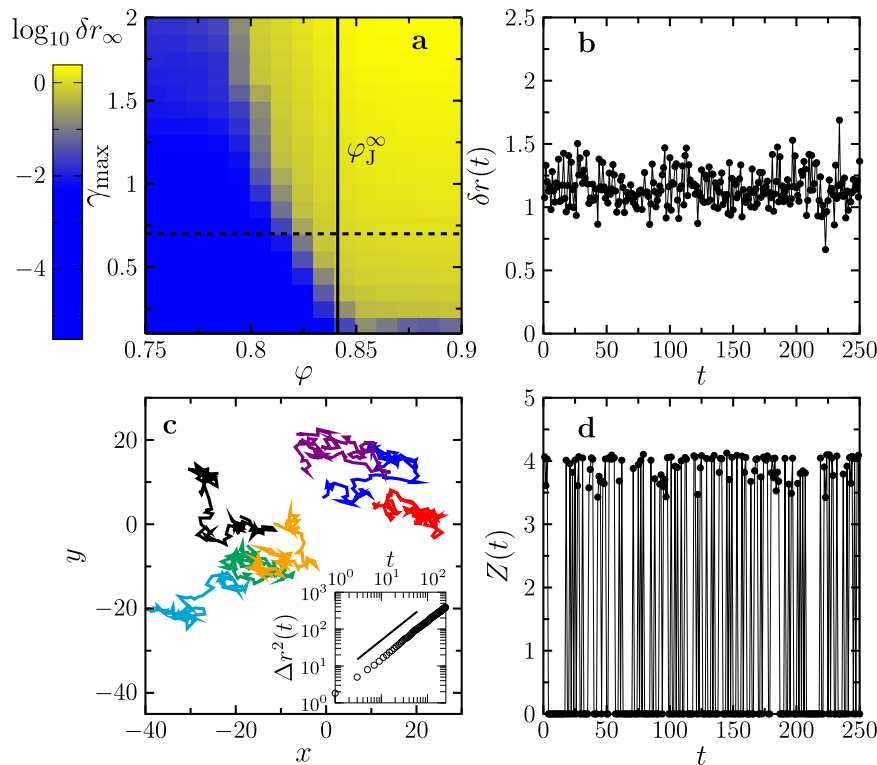


Fig. 1 | Cyclic athermal quasi-static shear simulations. **a** Reversible ($\Delta r_\infty < 0.1$, blue region) and irreversible ($\Delta r_\infty > 0.1$, yellow region) phases ($N = 1000$). The solid line represents $\varphi_j^\infty = 0.8432$, and the dashed line represents $\gamma_{\max} = 0.7$ used to generate the ensemble in the main text. **b** One-cycle displacement $\Delta r(t)$ and

d coordination number $Z(t)$ for a typical sample, at $\varphi = 0.841$. **c** Several typical particle trajectories during 100 cycles at $\varphi = 0.8425$. Positions are recorded at $y = 0$ only, and the system size is 43.8×43.8 with periodic boundary conditions. (inset) The MSD data show diffusive behavior $\langle \Delta r^2(t) \rangle \sim t$ (line).

transition is characterized by the one-cycle displacement averaged over particles⁵⁵,

$$\delta r(t) = \frac{1}{N} \sum_{i=1}^N |\mathbf{r}_i(t+1) - \mathbf{r}_i(t)|, \quad (1)$$

and the mean-squared displacement (MSD),

$$\langle \Delta r^2(t) \rangle = \frac{1}{N} \left\langle \sum_{i=1}^N |\mathbf{r}_i(t) - \mathbf{r}_i(0)|^2 \right\rangle, \quad (2)$$

where t is the number of cycles playing a similar role as the time in thermal systems, $\mathbf{r}_i(t)$ the position of particle i at time t and zero strain $\gamma = 0$, and $\langle x \rangle$ the average over N_s samples.

The RI dynamics near φ_j are systematically studied in ref. 55, according to which $\Delta r(t)$ displays two-step relaxation behavior typically appearing in glassy systems. For $\tau_R < t < \tau_L$, $\Delta r(t)$ develops a plateau at Δr_s . In the interested irreversible phase, $\Delta r_s > 0$, $\tau_R \rightarrow 0$ and $\tau_L > t_{\max}$ with t_{\max} the maximum simulation time, suggesting that the system reaches a stationary state (see Fig. 1b). In addition, the MSD in the irreversible phase shows typical diffusive behavior $\langle \Delta r^2(t) \rangle \sim t$ (see Fig. 1c). In contrast, in the reversible phase, $\Delta r_s = 0$, which means that the system is “absorbed” into an invariant state. In practice, one defines $\delta r_\infty = \delta r(t_{\max})$ and distinguish between the reversible and irreversible phases by comparing the value of Δr_∞ to a threshold Δr_{th} . In this study, we set $t_{\max} = 4000$ and $\Delta r_{\text{th}} = 0.1$, giving the boundary between irreversible (yellow) and reversible (blue) regions in Fig. 1a.

The above results imply that the configurational space is effectively explored by the dynamical trajectory of the system in the irreversible phase, encouraging us to consider a statistical ensemble generated by shear dynamics. In this study, we fix $\gamma_{\max} = 0.7$ unless otherwise specified, and vary φ systematically in the window of

[0.833, 0.849]. At each φ , in total $t_{\max} \times N_s$ independent configurations are generated to construct the ensemble. In the SI, we present additional results obtained for $\gamma_{\max} = 1$. All configurations are collected at $\gamma = 0$, which have weak anisotropy characterized by a non-zero average macroscopic friction coefficient (the ratio between stress and pressure), $\langle \sigma/P \rangle \approx 0.08$.

Figure 1d shows the evolution of the coordination number $Z(t)$ in the irreversible phase, obtained from a typical simulation near φ_j . Rattlers (particles with fewer than $d + 1$ contacts) are removed in the computation of Z . At first glance, one sees the coexistence of jammed ($Z \approx 2d = 4$) and unjammed states ($Z = 0$), similar to the coexistence of two ferromagnetic states (positive m and negative m) in the time evolution of the magnetization $m(t)$ in an Ising model near a first-order phase transition⁵⁸. However, a more careful examination reveals four distinct states, which we discuss in the next section.

It is well known now that the jamming density φ_j is not unique and protocol-dependent^{6,44,47–49,56,59,60} (In this study, φ_j denotes the J-point density that is the minimum jamming density, and φ_j denotes the protocol-dependent jamming density): In the compression protocol, φ_j depends on the compression rate or the density of the initial equilibrium configuration^{48,49}; in the cyclic athermal quasistatic compression (CAQC) protocol, φ_j depends on the volumetric strain amplitude (the maximum density φ_{\max} to which the system is compressed) and the number N_c of cycles^{44,59}; in the CAQS protocol, φ_j depends on the shear strain amplitude γ_{\max} and N_c ^{56,60}. The continuous range of possible φ_j is called a jamming-line (J-line), and the minimum jamming density on the J-line is the J-point density φ_j realized by rapid quenching⁶⁰. The protocol dependence of φ_j in the current model has been investigated in ref. 59 using the CAQC protocol, and the maximum jamming density obtained there is $\varphi_j \approx 0.8465$ after one over-compression cycle, compared to $\varphi_j \approx 0.842–0.843$. In order to examine the effects of non-universal φ_j , in this study, we prepare two types of

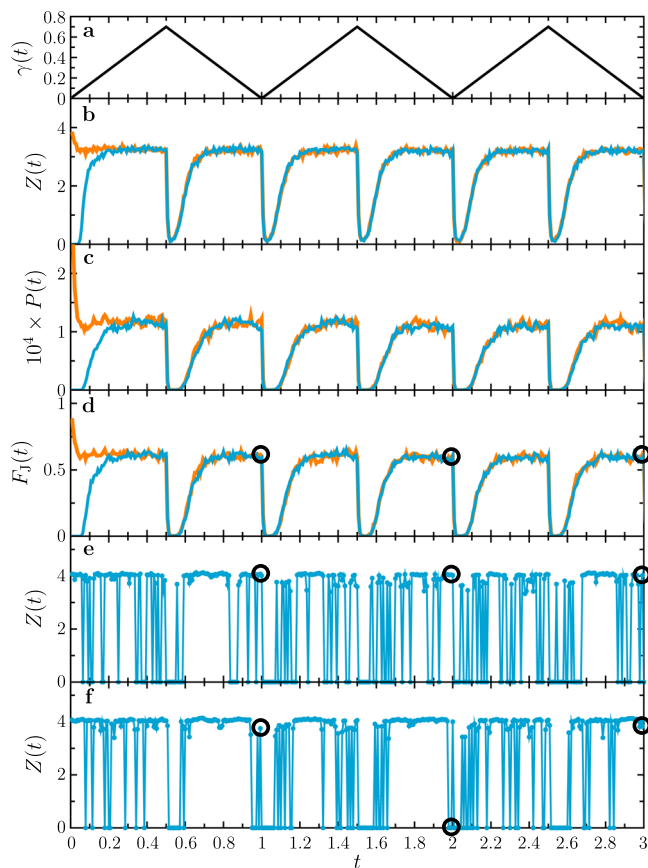


Fig. 2 | First three shear cycles. The **a** strain γ , **b** sample-averaged coordination number Z , **c** sample-averaged pressure P , and **d** jamming fraction F_j are plotted as functions of t during the first three shear cycles ($\varphi = 0.8425$, $N_s = 768$ samples). Orange and blue curves are obtained from rapidly quenched ($\varphi_j = \varphi_j \approx 0.843$) and mechanically trained ($\varphi_j \approx 0.848$) initial configurations respectively. The jamming fraction F_j used in the scaling analysis is obtained at $\gamma = 0$ (black circles in **d**). **e**, **f** Plotted is the $Z(t)$ of two typical samples initially generated by rapid quenching. The system status at $\gamma = 0$ is highlighted by black circles, which fluctuate among jammed ($Z \geq 4$), fragile ($3 < Z < 4$) and unjammed ($Z = 0$) states.

samples: rapidly quenched samples with $\varphi_j = \varphi_j \approx 0.843$, and mechanically trained samples generated by the CAQC protocol with $\varphi_j = 0.8479(4) > \varphi_j$.

The protocol dependence of φ_j is called a memory effect in ref. 44. Below we demonstrate that the cyclic shear simulation employed in this study erases the memory of the initial state: given the initial $\varphi_j \approx 0.848 > \varphi_j$, the jamming density reduces to $\varphi_j \approx 0.843$ after one complete shear cycle. Figure 2b–d shows the evolution of the sample-averaged coordination number Z , the sample-averaged pressure P , and the jamming fraction F_j of all considered samples at the given t . The differences between the curves of rapidly quenched ($\varphi_j \approx 0.843$) and mechanically trained systems ($\varphi_j \approx 0.848$) only appear in the first cycle. Thus the effect of the variable φ_j is eliminated during the construction of the ensemble by cyclic shear. Previous studies have shown that, independent of the initial jamming density φ_j , if the system is sheared by large strain deformations beyond the yield strain γ_Y , it always evolves into a critical steady state that has a generic jamming density at φ_j , and such a process is accompanied with significant shear dilatancy or hardening effects^{24,60,61}. According to Fig. 2b–d, the system has indeed reached the steady state before the strain reversal, as the strain amplitude $\gamma_{\max} = 0.7$ is larger than the yield strain $\gamma_Y \approx 0.1$.

Next we illustrate that the statistical properties of the ensemble are determined by fluctuation effects. The overall behavior of the

sample-averaged $Z(t)$ and $P(t)$ is very similar to that reported in previous cyclic shear simulations^{44,62}: one observes periodic patterns with the sharp onset of unjamming upon strain reversal at integer or half-integer t . However, no regular patterns can be identified in single-sample curves, which look more like stochastic processes (see Fig. 2e, f). Similar behavior has been observed in previous simple shear simulations⁴⁰ and experiments⁶³, showing that the coexistence of jammed and unjammed states during shear is a generic property of the system, at a fixed φ near the jamming transition. It is useful to consider two types of fluctuations. (i) Fluctuations between different cycles in the simulation of a given sample. The configurations at consecutive strain steps t and $t + \Delta t$ are related by both affine and non-affine deformations. Due to non-affine deformations, the two finite-size configurations can have different structures and jamming densities φ_j^N . If the preset constant density φ in the CAQS simulation is close to the average φ_j , then the two consecutive configurations can be either jammed ($\varphi_j^N < \varphi$) or unjammed ($\varphi_j^N > \varphi$). This fluctuation effect is the origin of stochastic-like behavior in Fig. 2e–f. (ii) Sample-to-sample fluctuations at a given t . For similar reasons, at a given t , two individual samples can be either jammed or unjammed due to sample-to-sample fluctuations (see marked points at the integer t in Fig. 2e, f). The jamming fraction F_j due to such sample-to-sample fluctuations is plotted in Fig. 2d, whose scaling behavior is analyzed in detail below. Note that the fluctuations in (i) and (ii) essentially have the same origin: in finite-size systems, the jamming density φ_j^N has a distribution $p(\varphi_j^N)$ due to the existence of abundant amorphous states.

As shown in Fig. 2d, upon on the strain reversal, F_j rapidly decays to zero, which means that the configuration jammed along a given shear direction is unstable to reverse shear deformations^{44,64,65}. This reversal-unjamming effect occurs within a strain interval $\Delta\gamma \lesssim 0.2$, and after this interval F_j reaches a stationary plateau. Because of the maximum strain $\gamma_{\max} > 0.2$ in our protocol, the configurations collected in the ensemble are always in the stationary regime.

Four states: unjammed, jammed, partially crystallized and fragile

In Fig. 3a, we plot the probability distribution $p(Z)$ of the states in the considered ensemble, at a fixed $\varphi = 0.841$ in the irreversible phase. The following four states, represented by peaks in $p(Z)$, can be identified (see Fig. 3e–h).

- (i) *Unjammed states.* The left-most peak is a delta-function $p_U(Z) - \Delta(Z)$, corresponding to unjammed states. All unjammed states have strictly zero contacts, $Z = 0$, once rattlers are removed.
- (ii) *Jammed states.* The right-most peak $p_J(Z)$ at $Z \geq 4$ corresponds to jammed states. Their average coordination numbers satisfy minimally the isostatic condition, $Z \geq 2d = 4$.
- (iii) *Partially crystallized states.* The delta-peak at $p_C(Z) - \Delta(Z - 24/7)$ represents the states with a single unit cell of the hexagonal crystal (see Fig. 3e). Here $24/7 \approx 3.4286$ is the average number of contacts of the seven particles forming the unit cell. Occasionally, states with two or three unit crystal cells can be also found but they are rare.
- (iv) *Fragile states.* We define the states in the broad peak $3 < Z < 4$, excluding the crystalline peak $p_C(Z)$, as the fragile states.

The fractions, F_U , F_J , F_C and F_F , of the above four states (i–iv), are obtained by integrating corresponding peaks in $p(Z)$. In Fig. 3b, the fractions are plotted as functions of φ , showing that $F_J(\varphi)$ increases from zero to one across φ_j . This behavior is quantitatively similar to $F_j(\varphi)$ obtained in previous rapid quench simulations, where finite-size analyses have been carried out to precisely determine the asymptotic jamming transition density φ_j^∞ in the thermodynamic limit $N \rightarrow \infty$ ^{2,41}. We will perform such finite-size analyses later, after discussing the nature of fragile states.

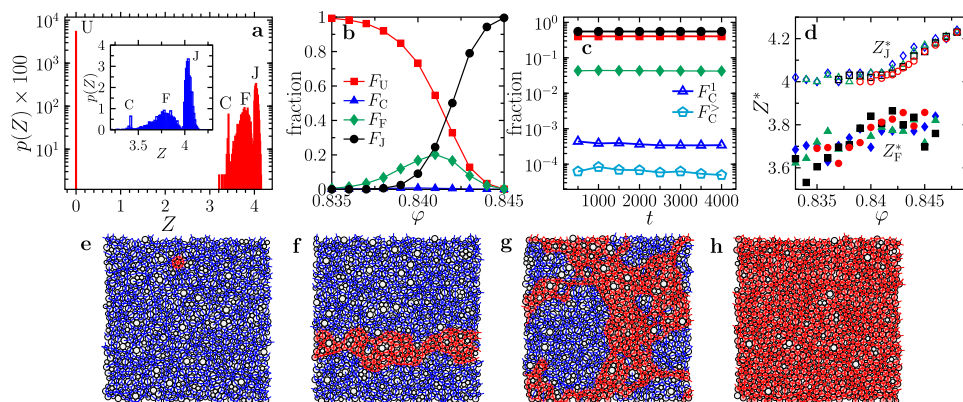


Fig. 3 | Four states. **a** Semi-log plot of the probability distribution $p(Z)$. The four peaks of unjammed (U), partially crystallized (C), fragile (F) and jammed (J) states, are indicated. The inset shows a linear plot of $p(Z)$ without the unjammed peak. Fractions are plotted as a function of ϕ in **b**, and of t in **c**. **e** each data point is obtained for a small window $[t-\Delta t, t+\Delta t]$ with $\Delta t = 250$. **d** Peak coordination numbers Z_J^* of jammed states (upper branch, open symbols) and Z_F^* of fragile states (lower branch, filled symbols) as functions of ϕ , for $N = 256$ (diamonds), 512

(triangles), 1000 (squares), and 2000 (circles). **e–h** we show typical configurations of **e** partially crystallized, **f** fragile percolating in one direction, **g** fragile percolating in both directions, and **h** jammed states. Contact forces are represented by bonds, whose width is proportional to the magnitude of force. The red and blue disks are non-rattler and rattler particles respectively. We set $\phi = 0.841$ for **a** and **c**, $N = 256$ for **b** and **c**, and $N = 1000$ for **a**, **e–h**.

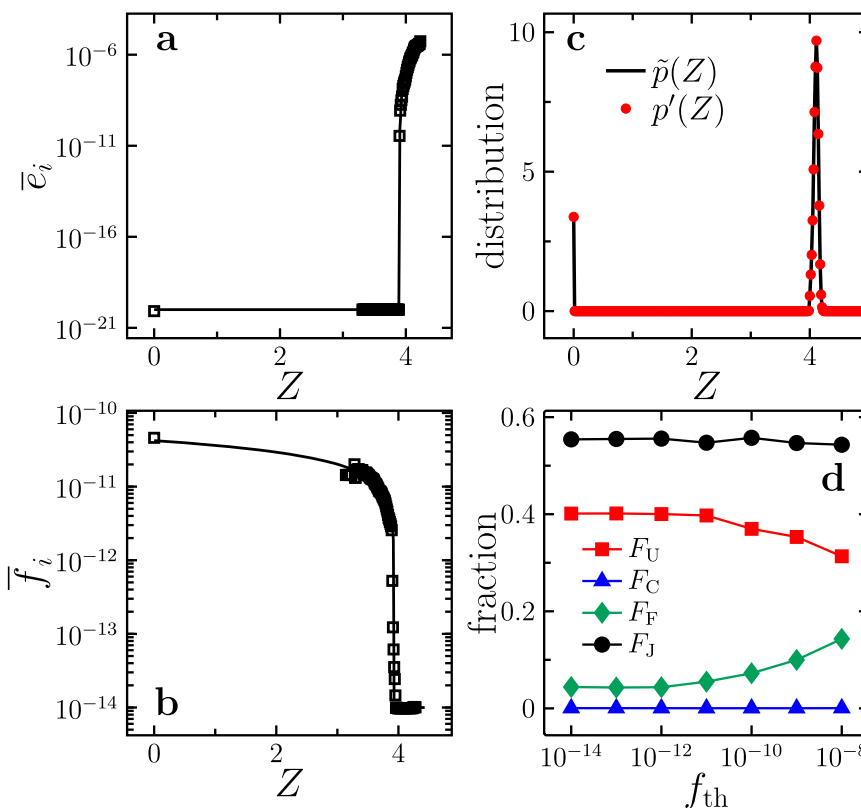


Fig. 4 | Stability tests. Average single-particle **a** potential energy \bar{e}_i and **b** net force \bar{f}_i as functions of Z . Lines in **a** and **b** are guides to the eye. **c** Comparison between $\tilde{p}(Z)$ obtained after the compression-decompression perturbation and $\bar{p}(Z)$ with

fragile states counted as unjammed states, for $N = 1000$ at $\phi = 0.844$. **d** Fractions of four states as functions of f_{th} . Data are obtained for $N = 256$ systems at $\phi = 0.841$, except for **c**.

In Fig. 3c, we report various fractions as functions of t at $\phi = 0.841$. The fractions are independent of t , confirming that the system is stationary. We further divide $F_C(t)$ into two parts, $F_C(t) = F_C^1(t) + F_C^>(t)$, where $F_C^1(t)$ and $F_C^>(t)$ are respectively the fractions of partially crystallized states with one and more than one crystal unit cells. Both $F_C^1(t)$ and $F_C^>(t)$ are independent of t , indicating that the growth of seed crystals is not observed. Because F_C is generally several orders of

magnitude lower than the fractions of other types, partially crystallized states will be ignored in the following analyses.

In Fig. 3d, we plot the maximum coordination numbers, Z_J^* and Z_F^* , of jammed and fragile peaks. Around ϕ , there is a small gap $\Delta Z_{gap} \approx 0.2$ between Z_J^* (upper branch) and Z_F^* (lower branch). The results are very similar to those obtained by quasistatic uniform shear in ref. 40 (see Fig. 4 therein). In ref. 40, it is suggested that ΔZ_{gap} vanishes in the

thermodynamic limit, and thus the jamming transition is continuous. However, as we show below, the fragile states are generated due to incomplete energy minimization and are mechanically unstable. Once such fragile states are excluded, the lower branch only contains unjammed states with $Z_{\text{U}}^* = 0$, which is separated by a large gap $\Delta Z_{\text{gap}} \approx 4$ from the upper branch $Z_{\text{J}}^* \geq 4$.

Instability of fragile states

Previously, the fragile states were obtained by uniform shear at non-zero strains $\gamma > 0$ below φ_{J} in experiments⁶⁶ and simulations⁴⁴. It was proposed that fragile and jammed states differ in the percolation of the strong force network: in fragile states the percolation occurs anisotropically in one direction only, while in jammed states it occurs isotropically in both directions. In this study, all states are collected during cyclic shear at $\gamma = 0$, and the fragile states with $3 < Z < 4$ can have percolated force networks of non-rattlers in one or two directions (see Fig. 3f, g). Thus in our case, anisotropy cannot effectively distinguish fragile from jammed states. It should be noted that, due to strong fluctuation effects, the fragile states can be generated either before or after jamming during the shear procedure (see Fig. 2e, f).

We demonstrate that the essential difference between fragile and jammed states is their mechanical stability. In fragile states, the potential energy per particle is negligibly low (see *Stopping criterion for energy minimization* in Methods), $\bar{e}_i < e_{\text{th}} = 10^{-20}$ (see Fig. 4a), but the fraction of non-rattler particles is non-zero. These non-rattlers experience forces, which can form a transient, percolated network. Such networks are highly heterogeneous (see Fig. 3f, g), compared to those in jammed states (see Fig. 3h). More importantly, the force networks in fragile states are unstable, revealed by the non-zero net force per particle, $\bar{f}_i > f_{\text{th}} = 10^{-14}$ (see Fig. 4b). Thus fragile states are not strictly equilibrated; they turn into unjammed states by sufficiently long relaxation (accurate energy minimization) or mechanical perturbations.

To demonstrate the instability of fragile states, two tests are carried out. First, we perform a compression-decompression perturbation, $\varphi \rightarrow \varphi + \Delta\varphi \rightarrow \varphi$, where $\Delta\varphi = 10^{-8}$, with the energy minimized after each step. All fragile states ($3 < Z < 4$) become unjammed ($Z = 0$) after this perturbation, while jammed states remain. In Fig. 4c, we plot the distribution $p'(Z)$ after the compression-decompression perturbation. Independently, without any perturbation we simply regard all fragile states ($3 < Z < 4$) as unjammed ($Z = 0$) and recalculate the distribution $\tilde{p}(Z)$. Figure 4c shows that the two distributions $p'(Z)$ and $\tilde{p}(Z)$ perfectly coincide.

In the second test, we repeat CAQS simulations by systematically varying the threshold f_{th} in the criterion of the energy minimization algorithm. The fraction F_{F} of fragile states grows and F_{U} of unjammed states decays with increasing f_{th} (Fig. 4d), suggesting that many unjammed states become fragile under a looser force-balance condition $\bar{f}_i < f_{\text{th}}$ with a larger f_{th} . In contrast, the constant F_{J} shows that the definition of jammed states is insensitive to the algorithm parameter. The $p(Z)$ data with different f_{th} confirm this property: the fragile peak depends on f_{th} while the jammed peak is independent of f_{th} (see SI Fig. S1a). Note that in granular experiments^{66,67}, the friction may play the role of f_{th} , i.e., the net inter-particle force could be balanced by the frictional force between particles and the supporting plate. According to this assumption, the probability of observing fragile states in experiments would depend on the particle-plate friction that can be changed by replacing the materials. It provides a protocol to examine our scenario of fragile states in future experimental studies.

Because fragile (and partially crystallized) states with $3 < Z < 4$ are unstable, from now on we count them as unjammed states. More specifically, we replace the original distribution $p(Z)$ with the modified distribution $\tilde{p}(Z)$. For simplicity, we omit the tilde and denote $\tilde{p}(Z)$ by $p(Z)$ below.

Scaling analysis near the jamming transition

Firstly, we outline the general strategy in the following scaling analyses. In particular, the effects of disorder on a first-order phase transition shall be specified. Near a first-order phase transition, the probability distribution $p(m)$ of the order parameter m has two well-separated peaks corresponding to two phases^{58,68}, $p(m) = p_1(m) + p_2(m)$. The fractions of the two phases are respectively, $F_1 = \int p_1(m) dm$ and $F_2 = \int p_2(m) dm$, satisfying $F_1 + F_2 = 1$. In the thermodynamic limit $N \rightarrow \infty$, $F_1(x)$ and $F_2(x)$ are sharp step functions of the control parameter x (for example, the temperature T), which jump discontinuously at the transition point x_c . In finite-size systems, $F_1(x, N)$ and $F_2(x, N)$ turn into smooth functions due to fluctuations, and usually a finite-size scaling analysis becomes necessary to determine the nature of the transition. Near x_c , the fraction $F_1(x, N)$ (or $F_2(x, N)$) follows a scaling form, $F_1(x, N) = \mathcal{F}_1[(x - x_c)N^\lambda]$, where the value of λ depends on whether disorder presents. It is also illustrative to study the behavior of the connected susceptibility $\chi_{\text{con}} = d\langle m \rangle / dx$ and the disconnected susceptibility $\chi_{\text{dis}} = N(\langle m^2 \rangle - \langle m \rangle^2)$. The scalings are unambiguously distinguishable in the following two types of first-order phase transitions.

- (I) Standard first-order transitions without disorder. In this case, $F_1(x, N)$ has the scaling form $F_1(x, N) = \mathcal{F}_1[(x - x_c)N]$. The fluctuation-dissipation theorem ensures that the susceptibility can be equivalently computed from the response or from the fluctuations, i.e., $\chi_{\text{dis}} = \chi_{\text{con}}$. Examples in this category include the first-order transition in the q -state Potts model with $q > 4$ where the control parameter is the temperature T , and that in the Ising model driven by an external magnetic field h at temperatures below the critical temperature.
- (II) First-order transitions in disordered systems driven by an external field, where sample-to-sample fluctuations due to disorder are significantly stronger than thermal fluctuations and the system can be effectively considered as athermal ($T = 0$). The scaling form of $F_1(x, N)$ is $F_1(x, N) = \mathcal{F}_1[(x - x_c)N^{1/2}]$. The exponent $\lambda = 1/2$ originates from the finite-size scaling of the standard deviation of the transition point $\Delta x_c \sim N^{-1/2}$ due to the presence of disorder. The two susceptibilities are related by, $\chi_{\text{dis}} \sim \chi_{\text{con}}^2 \sim N^{69}$, where the average $\langle \dots \rangle$ in the definition of susceptibilities should be taken over disorder realizations. A paradigm transition in this type is the non-equilibrium first-order transition in the athermal random-field Ising model (RFIM) driven by an external field $h^{70,71}$. Other examples include the brittle yielding in amorphous solids under strain γ deformations^{71,72}, and the melting of ultrastable hard-sphere glasses under decompression⁷³.

For the interested jamming transition, the control parameter is φ , by tuning which continuously the jamming transition occurs, and the order parameter is Z , which characterizes the jammed ($Z > 4$) and unjammed phases ($Z = 0$). They are analogous to the external field h and the magnetization m in the athermal driven RFIM in type (II). The transition is between unjammed and jammed phases, represented by two separated peaks in the distribution $p(Z)$. The fractions of unjammed and jammed states are $F_1(\varphi, N) = F_{\text{U}}(\varphi, N)$ and $F_2(\varphi, N) = F_{\text{J}}(\varphi, N)$ respectively. The disconnected susceptibility is defined as, $\chi_{\text{dis}} \equiv N\sigma_Z^2 = N(\langle Z^2 \rangle - \langle Z \rangle^2)$, where σ_Z^2 is the variance of $p(Z)$ and $\langle \dots \rangle$ is the average over all states. The connected susceptibility is defined as $\chi_{\text{con}} = d\langle Z \rangle / d\varphi$. Below, we analyze in detail the simulation data of $F_1(\varphi, N)$, $\chi_{\text{dis}}(\varphi, N)$ and $\chi_{\text{con}}(\varphi, N)$, demonstrating that they satisfy the scalings in (II). Note that the disorder may have different origins in type (II) transitions. In RFIM, the disorder corresponds to the quenched random local fields in the definition of the Hamiltonian, while for the jamming transition, the disorder is due to the amorphous configuration of particle arrangements.

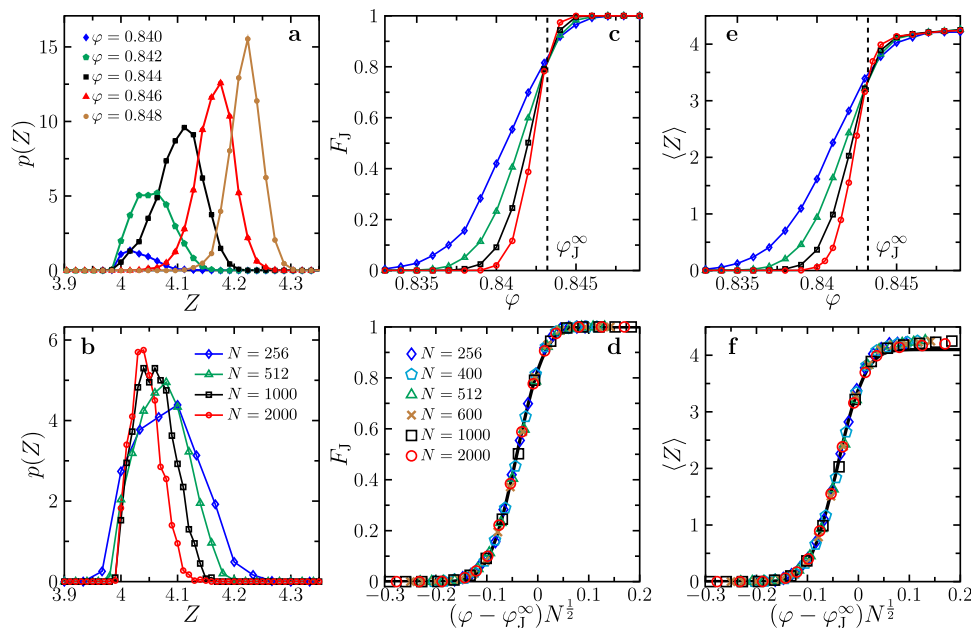


Fig. 5 | Distribution of the coordination number. **a** Probability distribution $p(Z)$ at a few different φ for $N=1000$. **b** $p(Z)$ at $\varphi=0.843$ for a few different N . For better visualization, we do not show the unjammed delta-peak at $Z=0$ (see SI Fig. S1b for full distributions). **c** The fraction of jammed states F_J as a function of φ for a few different N . The intersection of curves gives $\varphi_J^\infty = 0.8432(2)$. **d** The data points of F_J

with different N collapse as a function of $(\varphi - \varphi_J^\infty)N^{1/2}$. The solid line represents fitting to Eq. (4), with two fitting parameters $u = 0.041(1)$ and $\sigma_\varphi = 0.043(1)$. The average coordination number $\langle Z \rangle$ is plotted as a function of φ in **e** and of $(\varphi - \varphi_J^\infty)N^{1/2}$ in **f**. The solid line in **f** represents $\langle Z \rangle = F_J Z_J^*$ using $u = 0.041$, $\sigma_\varphi = 0.043$ and $Z_J^* = 4.1$. Symbols in **b–f** have the same meanings.

In Fig. 5a, b, we plot $p(Z)$ for a few different φ and N , showing that $p(Z)$ is always double-peaked across the jamming transition (see SI Fig. S1b), which is typical behavior of a first-order rather than a second-order transition. To analyze the scaling behavior of $p(Z)$, we consider a general form of first-order phase transitions^{58,68},

$$p(Z) = (1 - F_J)\delta(Z) + F_J p_J \left[(Z - Z_J^*)N^\eta \right], \quad (3)$$

where $\Delta(Z)$ and $p_J(Z)$ correspond to the unjammed and jammed peaks respectively. The asymptotic jamming density $\varphi_J^\infty = 0.8432(2)$ for $N \rightarrow \infty$ is determined by the intersection of $F_J(\varphi)$ curves with different N (see Fig. 5c). This value is consistent with the J-point density $\varphi_J \approx 0.842\text{--}0.843$ given by previous studies^{2,41}, which is unambiguously below the maximum protocol-dependent jamming density $\varphi_J \approx 0.8465$ reported in ref. 59 and $\varphi_J \approx 0.848$ obtained by CAQC in this study. The difference between $\varphi_J^\infty = 0.8432(2)$ by $\gamma_{\max} = 0.7$ and $\varphi_J^\infty = 0.8435(1)$ by $\gamma_{\max} = 1$ (see SI Figs. S2b and S3, 4) is too small to conclude any systematic dependence on γ_{\max} . In ref. 56, an unjamming pocket is reported in the phase diagram for $\gamma_{\max} < 0.17$, while for larger γ_{\max} , φ_J is independent of γ_{\max} , consistent with our observations. These results also suggest that the jamming density obtained by cyclic shear is the lowest jamming density on the J-line of all possible jammed states^{6,48,60}. We emphasize that $\gamma_{\max} = 0.7$ in this study is significantly larger than the yield strain $\gamma_Y \approx 0.1$ (see SI Fig. S5a). For a small strain amplitude, $\gamma_{\max} = 0.05$, we observe a logarithmic growth of φ as a function of t under a constant pressure condition^{44,74}, suggesting that the jamming density can be increased by cyclic shear with a small γ_{\max} ^{56,60}; in contrast, for $\gamma_{\max} = 0.7$, φ remains as a constant (see SI Fig. S5b).

As shown in Fig. 3d, Z_J^* is independent of N near φ_J , and weakly depends on φ . In the following scaling analysis, Z_J^* is approximated by a constant value $Z_J^* = 4.1(1)$ at $\varphi_J^\infty = 0.8432$. To keep the expressions concise, we ignore the corrections to the scaling functions from the φ -dependence of Z_J^* .

We assume the fraction of jammed states F_J having the following scaling form, $F_J(\varphi, N) = \mathcal{F}_J \left[(\varphi - \varphi_J^\infty)N^\lambda \right]$. The value of the exponent λ is

important for understanding the nature of the transition. If the system were thermal, the fraction would be determined by the Boltzmann distribution, $F_J \sim \exp\left(\frac{N\Delta f}{k_B T}\right)$, where Δf is the single-particle free energy difference between two phases^{58,68}. Because the free energy is non-singular around a first-order phase transition, it can be expanded, giving $\Delta f \sim (T - T_c)$ to the lowest order. Thus, if the jamming transition were a standard first-order phase transition, then $F_J(\varphi, N) = \mathcal{F}_J \left[(\varphi - \varphi_J^\infty)N \right]$, i.e., $\lambda = 1$ (note that φ is the control parameter of the jamming transition). However, our numerical data cannot be collapsed using $\lambda = 1$; in contrast, they can be perfectly collapsed using $\lambda = 1/2$ (see Fig. 5d).

To understand the origin of $\lambda = 1/2$ scaling, recall that the athermal jamming transition is not driven by the free energy difference between the two phases. Below we explain the scaling by the scenario of a first-order transition with quenched disorder. For a finite N , due to the presence of disorder in the packing structure, the jamming density φ_J^N should fluctuate around the asymptotic value φ_J^∞ . Let us assume a simple Gaussian form of the distribution, $\rho(\varphi_J^N) \sim \exp\left[-\frac{(\delta\varphi_J + u)^2}{2\sigma_\varphi^2}\right]$, where $\delta\varphi_J = (\varphi_J^N - \varphi_J^\infty)N^{1/2}$ follows the standard central limit theorem. Note that $\rho(\varphi_J^N)$ has been explicitly measured in the compression protocol^{2,57}: the width of $\rho(\varphi_J^N)$ scales as $w \sim N^{-0.55}$ in both 2D and 3D, supporting our assumption. The above assumption also predicts, $\varphi_J^N - \varphi_J^\infty \sim N^{-1/2}$, independent of the dimensionality. The jammed states are defined by $\varphi > \varphi_J^N$, and thus

$$F_J(\varphi, N) = \int_0^\varphi \rho(\varphi_J^N) d\varphi_J^N \approx \frac{1}{2} + \frac{1}{2} \operatorname{erf} \left[\frac{\delta\hat{\varphi} + u}{\sqrt{2}\sigma_\varphi} \right], \quad (4)$$

where $\delta\hat{\varphi} = (\varphi - \varphi_J^\infty)N^{1/2}$. Equation (4) agrees well with the data in Fig. 5d. The dependence of $F_J(\varphi, N)$ on shear parameters is examined in Fig. S2. The $F_J(\varphi, N)$ data are independent of the maximum strain γ_{\max} , and weakly depend on the strain step $\Delta\gamma$. Independent of $\Delta\gamma$, the $F_J(\varphi, N)$ data of different N collapse when plotted as a function of the rescaled

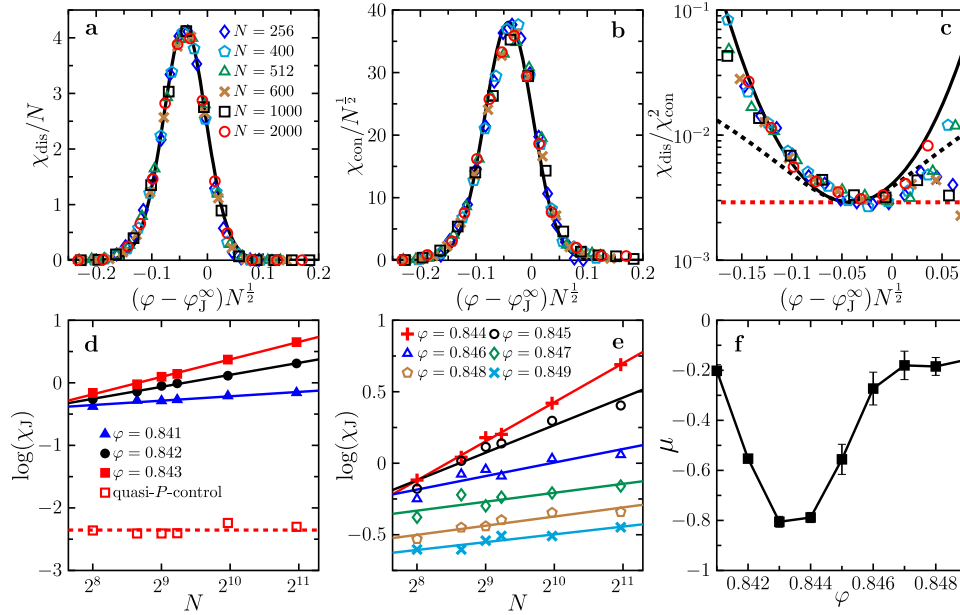


Fig. 6 | Susceptibilities. We plot **a** the disconnected susceptibility χ_{dis} rescaled by N , **b** the connected susceptibility χ_{con} rescaled by $N^{1/2}$, and **c** the ratio between χ_{dis} and χ_{con}^2 , as functions of $(\varphi - \varphi_j^\infty)N^{1/2}$. The solid black lines in **a–c** are Eqs. (5), (6), and the ratio between Eq. (5) and the square of Eq. (6), respectively. The dashed black line in **c** is the second-order expansion Eq. (7). The dashed red line in **c** is the constant term in Eq. (7), i.e., $\chi_{\text{dis}}/\chi_{\text{con}}^2 = \pi\sigma_\varphi^2/2$. To draw these lines, we use $u = 0.041$ and $\sigma_\varphi = 0.043$ obtained from the fitting in Fig. 5d, and $Z_j^* = 4.1$ determined at

$\varphi_j^\infty = 0.8432$ in Fig. 3d. No fitting is performed here. Symbols in **a–c** have the same meanings as indicated in the legend of **a**. **d, e** the susceptibilities of jammed states χ_j are plotted as functions of N for a few different φ , and are fitted to Eq. (8). The open squares in **d** are χ_j data obtained in a small pressure window $0.0009 < P < 0.0011$, corresponding to $\Delta Z \approx 0.15$ ($\varphi \approx 0.843–0.844$). The fitting parameter μ is plotted in **f** as a function of φ , where the error bar represents the fitting error.

variable $(\varphi - \varphi_j^\infty)N^{1/2}$ (see Figs. 5d and S2c for $\Delta\gamma = 10^{-2}$ and 10^{-1} respectively), showing robustness of the scaling function Eq. (4).

Once the scaling behavior of $F_j(\varphi, N)$ is obtained, it is easy to derive scaling forms of susceptibilities. From Eq. (3) and the definition of χ_{dis} , we obtain,

$$\frac{\chi_{\text{dis}}(\varphi, N)}{N} \approx (Z_j^*)^2 [1 - F_j(\varphi, N)] F_j(\varphi, N), \quad (5)$$

where $F_j(\varphi, N)$ is given by Eq. (4). Equation (5) suggests a scaling form $\chi_{\text{dis}}(\varphi, N)/N = \mathcal{X}_{\text{dis}}[(\varphi - \varphi_j^\infty)N^{1/2}]$, in agreement with the data in Fig. 6a.

From Eq. (3), one finds that $\langle Z \rangle \approx F_j Z_j^*$ and thus $\langle Z \rangle$ has the same scaling form as F_j , i.e., $\langle Z \rangle(\varphi, N) = \mathcal{Z}[(\varphi - \varphi_j^\infty)N^{1/2}]$, consistent with the data in Fig. 5e, 5f. Using $\chi_{\text{con}} = Z_j^* \frac{dF_j}{d\varphi}$ and Eq. (4), we obtain,

$$\frac{\chi_{\text{con}}(\varphi, N)}{N^{1/2}} \approx \frac{Z_j^*}{\sigma_\varphi \sqrt{2\pi}} \exp \left[- \left(\frac{\delta\hat{\varphi} + u}{\sqrt{2}\sigma_\varphi} \right)^2 \right], \quad (6)$$

which is verified by the simulation data in Fig. 6b.

Now we can look at the relationship between χ_{dis} and χ_{con} . Expanding Eqs. (5) and (6) around the maxima, where $x \equiv \frac{\delta\hat{\varphi} + u}{\sqrt{2}\sigma_\varphi} = 0$, we obtain, up to the quadratic order,

$$\frac{\chi_{\text{dis}}}{\chi_{\text{con}}^2} \approx \frac{\pi\sigma_\varphi^2}{2} \left[1 + \left(2 - \frac{4}{\pi} \right) \left(\frac{\delta\hat{\varphi} + u}{\sqrt{2}\sigma_\varphi} \right)^2 \right]. \quad (7)$$

To the lowest order, Eq. (7) gives a scaling $\chi_{\text{dis}} \sim \chi_{\text{con}}^2$, which is a key signature of the presence of quenched disorder. Comparing to the simulation data, Eq. (7) works well around the extreme point (see Fig. 6c). The agreement can be improved using higher-order expansions.

It seems that the non-Gaussian effect in the distribution $\rho(\varphi_j^N)$, which is neglected in the present analysis, is amplified in the data of $\chi_{\text{dis}}/\chi_{\text{con}}^2$, resulting in slight asymmetry. In SI Figs. S3, 4 and S6, 7, we show that the scaling functions Eqs. (4)–(7) work in 3D, and for a different max strain $\gamma_{\text{max}} = 1$ in 2D. In 3D, we obtain $\varphi_j^\infty = 0.6479(2)$, consistent with the previously reported J-point density $\varphi_j \approx 0.648$ of this model⁵⁶, which is the minimum jamming density on the J-line. For the same 3D model, the protocol-dependent jamming density is obtained up to $\varphi_j = 0.6616$ by the thermal annealing method⁴⁸, and up to $\varphi_j = 0.661$ by the CAQS mechanical training method⁵⁶.

Next let us discuss the finite-size effects of the jammed peak $p_j(Z)$ in Eq. (3). For standard first-order phase transitions, $\eta = 1/2$ ^{58,68}. Thus in that scenario the susceptibility of the jamming peak would scale as, $\chi_j \equiv N\sigma_j^2 = N(\langle Z - Z_j^* \rangle^2)_j \sim \text{constant}$, where σ_j^2 is the variance of $p_j(Z)$ and $\langle \dots \rangle_j$ represents the average restricted to the jammed states only. However, our χ_j data disagree with this scaling (see Fig. 6d–f). At different φ , χ_j can be fitted to a power-law form $\chi_j \sim N^{-\mu}$ ^{25,26}, or

$$\chi_j \sim N^{-\mu/d}, \quad (8)$$

where $N \sim \ell^d$. The exponent $\mu = d(2\eta - 1)$ is a fitting parameter. At large or small φ away from φ_j^∞ (see Fig. 6f), the exponent is close to zero ($\mu \approx -0.2$), suggesting that the local coordination numbers Z_i are uniformly distributed. The deviation from the uncorrelated behavior ($\mu = 0$) is significant around φ_j^∞ , where $\mu \approx -0.8$ reaches the minimum.

The result of μ shall be interpreted with care. In general, (i) $\mu = 0$ corresponds to uniformity of Z_i , (ii) $\mu > 0$ to hyperuniformity with a vanishing χ_j in the thermodynamic limit, and (iii) $\mu < 0$ to hyperfluctuations with a diverging χ_j in the thermodynamic limit that typically appears at the critical point in a second-order phase transition. However, the negative μ in Fig. 6f is not due to the criticality of the jamming transition. Here it is essential to consider the volume fluctuations. The negative μ is obtained from a φ -controlled setup in our

CAQS simulations. If we instead select configurations around a constant pressure P , then the fluctuations become significantly smaller, and $\mu \approx 0$ (Fig. 6d). This observation is consistent with a previous study⁷⁵, suggesting that the large fluctuation of Z near φ_j^∞ in the φ -controlled protocol might be originated from the fluctuation of φ_j^N . In fact, careful measurement gives $\mu \approx 1$ in a P -controlled protocol at jamming, confirming hyperuniformity^{25,26}. Ref. 26 also compares an ensemble of subsystems cut out from large packings, to an ensemble of whole systems with the same volume under periodic boundary conditions (similar to the P -controlled ensemble considered in this study): the contact fluctuations in the former are larger than those in the latter, and the convergence of these two are expected to occur in extremely large systems that are not attainable in current simulations—due to this pre-asymptotic effect, the hyperuniform exponent $\mu \approx 1$ is only observable in the first ensemble, while in the second ensemble, the apparent exponent is close to $\mu \approx 0$, consistent with our P -controlled data in Fig. 6d. In short, although the hyperuniform exponent $\mu = 1$ is not directly observed, our results do not contradict the recently reported hyperuniform behavior of contact distributions at jamming. We emphasize that the finite-size effects of the jammed peak $p_j(Z)$ contribute negligibly to the scaling of $F(\varphi, N)$, $\chi_{\text{dis}}(\varphi, N)$, and $\chi_{\text{con}}(\varphi, N)$. In other words, the first-order nature of the jamming transition is independent of how Z_i is spatially distributed in jammed packings.

In the scaling analysis presented above, Z is treated as the essential order parameter. In principle, the same kind of scaling analysis can be applied to any physical quantity A that varies discontinuously at jamming (e.g., A can be the bulk modulus B or the fraction of non-rattlers f_{NR}). The distribution $p(A)$ should have the same form as Eq. (3), $p(A) = (1 - F_j)\Delta(A) + F_j p_j(A)$. With fragile states removed, generally, $A = 0$ below jamming because no contacts are formed (e.g., $B = 0$ and $f_{\text{NR}} = 0$), and thus the unjammed peak is always a delta function. The fraction of jammed states F_j only depends on the constructed ensemble, which determines how the states are sampled, and thus its scaling form $F_j(\varphi, N) = \mathcal{F}_j[(\varphi - \varphi_j^\infty)N^{1/2}]$ is independent of A . The jammed peak $p_j(A)$ does depend on A , but as shown above, $p_j(A)$ is irrelevant to the interested scaling behavior of F_j , χ_{dis} and χ_{con} . Thus, our conclusion drawn from the scaling analysis should be robust and generic, independent of which parameter A is chosen for the scaling analysis, as long as A can reflect the discontinuous nature of jamming. If one instead chooses a continuous variable, such as the pressure P , then the above scaling analysis would not work.

Discussion

In this study, we investigate the nature of the jamming transition through an ensemble approach analogous to the statistical mechanics in equilibrium systems^{22,76}. Within such a framework, jamming is demonstrated to be a first-order transition with quenched disorder, in the quasistatic deformation limit where all fragile states are excluded. The order of the jamming transition is independent of the complex properties of jammed packings, including isostaticity, marginality and hyperuniformity (see (i–iii) in Introduction).

In previous rapid quench simulations, it is observed that the width w of the jamming density distribution $P(\varphi_j^N)$ scales as $w \sim N^{-\Omega}$ with $\Omega = 0.55 \pm 0.03$ in both 2D and 3D². This finite-size scaling depends on the total number of particles, N , rather than on the system length ℓ , and the exponent $\Omega \approx 1/2$ is independent of the dimensionality within the numerical accuracy. An explanation, as suggested previously, is that jamming is a second-order transition with an upper critical dimension $d_u = 2$ ³⁶. Here we propose an alternative interpretation: jamming is a first-order transition with quenched disorder, and consequently the finite-size scaling is a function of $(\varphi - \varphi_j^\infty)N^{1/2}$, independent of the dimensionality. We expect that the same finite-size scaling applies to the steady-state configurations generated by uniform simple shear.

It is of particular interest to reconcile the first-order transition established here under quasistatic shearing and the second-order transition observed in previous finite-rate rheology (see (iv) in Introduction). Conventionally, first- and second-order transitions coexist in gas-liquid systems, but not in liquid-crystalline solid systems. Because the liquid-crystalline solid transition is accompanied with spontaneous symmetry breaking, it cannot be a continuous type. However, there is no apparent spontaneous symmetry breaking during liquid-amorphous solid transitions (such as the jamming transition). Thus there is no fundamental reason to exclude the possibility of the coexistence of discontinuous and continuous transitions between a liquid and an amorphous solid. This study opens an avenue to unify first-order (this study) and second-order³⁷ jamming transitions.

In this study, we ignore thermal fluctuations. An interesting direction of the future work is to study the competition between the sample-to-sample fluctuations due to disorder and the fluctuations associated to the granular temperature^{62,77}, and examine the “thermal effects” on the nature of the first-order jamming transition. Similar studies on the thermal vestiges of the zero temperature physics have been recently carried out in the driven RFIM at finite temperatures⁷⁸. It would also be interesting to examine if friction can alter the order of the jamming transition^{79,80}.

Methods

Models

We study models of frictionless, bidisperse particles in two and three dimensions. The number ratio between large and small particles is 1:1, and the diameter ratio is 1.4:1. The potential energy between two particles is:

$$U(r_{ij}) = \frac{\epsilon}{2} \left(1 - \frac{r_{ij}}{\sigma_{ij}}\right)^2 \Theta\left(1 - \frac{r_{ij}}{\sigma_{ij}}\right), \quad (9)$$

where $\epsilon = 1$ is the energy unit, r_{ij} the distance between particles i and j , $\sigma_{ij} = \frac{\sigma_i + \sigma_j}{2}$ the mean diameter, and $\Theta(x)$ the Heaviside step function. We set unit particle mass, and the mean diameter as the unit length.

Shear protocol

Particles are randomly distributed at an initial volume fraction $\varphi_0 = 0.02$. The system is then rapidly quenched compressed to the target φ . The CAQS is performed under the Lees-Edwards boundary conditions⁸¹, with a fixed φ . The strain γ is varied stepwise, rather than continuously, between 0 and γ_{max} . We use a strain step $\Delta\gamma = 0.1$ to generate the phase diagram in Fig. 1a, and $\Delta\gamma = 0.01$ for other results. At each step, particle positions are shifted according to $x_i \rightarrow x_i + \Delta\gamma y_i$, and then the system's energy is minimized using the FIRE algorithm⁸². During a cycle, the strain is varied as $\gamma = 0 \rightarrow \gamma_{\text{max}} \rightarrow 0$. We set $\gamma_{\text{max}} = 0.7$ in the main text and $\gamma_{\text{max}} = 1$ in the SI for the 2D model, and $\gamma_{\text{max}} = 0.5$ for the 3D model (SI). The number of cycles is represented by t with unit oscillation period ($t = 1$). In 2D, the maximum number of cycles is $t_{\text{max}} = 250$ for $0.839 \leq \varphi \leq 0.849$ and $t_{\text{max}} = 4000$ for $0.833 \leq \varphi < 0.839$, while in 3D, $t_{\text{max}} = 144$ for 2000, and $t_{\text{max}} = 50$ for $N = 512$ and 1000. We generate $N_s = 4000$ –12,000 independent samples at each φ . At each φ , in total $t_{\text{max}} \times N_s$ configurations are collected to compute statistical quantities.

Stopping criterion for energy minimization

We terminate the energy minimization when the potential energy per particle $\bar{e}_i = \frac{1}{N} \sum_{i=1}^N e_i$ falls below a threshold e_{th} or the average single-particle net force $\bar{f}_i = \frac{1}{N} \sum_{i=1}^N f_i$ falls below f_{th} , whichever is satisfied earlier. We set $e_{\text{th}} = 10^{-20}$ and $f_{\text{th}} = 10^{-14}$ unless otherwise specified.

Data availability

Source data are provided with this paper.

Code availability

The simulation program is available at <https://github.com/dengpan-cn/Library-of-Athermal-Quasi-static-Shear-Simulation-of-Granular-Matter>.

References

- Makse, H. A., Johnson, D. L. & Schwartz, L. M. Packing of compressible granular materials. *Phys. Rev. Lett.* **84**, 4160 (2000).
- O'Hern, C. S., Silbert, L. E., Liu, A. J. & Nagel, S. R. Jamming at zero temperature and zero applied stress: the epitome of disorder. *Phys. Rev. E* **68**, 011306 (2003).
- Liu, A. J. & Nagel, S. R. The jamming transition and the marginally jammed solid. *Annu. Rev. Condens. Matter Phys.* **1**, 347–369 (2010).
- van Hecke, M. Jamming of soft particles: geometry, mechanics, scaling and isostaticity. *J. Phys. Condens. Matter* **22**, 033101 (2009).
- Pan, D., Wang, Y., Yoshino, H., Zhang, J. & Jin, Y. A review on shear jamming. *Phys. Rep.* **1038**, 1–18 (2023).
- Parisi, G. & Zamponi, F. Mean-field theory of hard sphere glasses and jamming. *Rev. Mod. Phys.* **82**, 789 (2010).
- Charbonneau, P., Kurchan, J., Parisi, G., Urbani, P. & Zamponi, F. Glass and jamming transitions: from exact results to finite-dimensional descriptions. *Annu. Rev. Condens. Matter Phys.* **8**, 265–288 (2017).
- Parisi, G., Urbani, P. & Zamponi, F. Theory of simple glasses: exact solutions in infinite dimensions (Cambridge University Press, 2020).
- Maxwell, J. C. I.—on reciprocal figures, frames, and diagrams of forces. *Earth Environ. Sci. Trans. R. Soc. Edinb.* **26**, 1–40 (1870).
- Alexander, S. Amorphous solids: their structure, lattice dynamics and elasticity. *Phys. Rep.* **296**, 65–236 (1998).
- Wyart, M. On the rigidity of amorphous solids. *Ann. Phys. Fr.* **30**, 1–96 (2005).
- Wyart, M., Sidney, & R. Nagel, S.R. Witten, T.A. Geometric origin of excess low-frequency vibrational modes in weakly connected amorphous solids. *Europhys. Lett.* **72**, 486 (2005).
- Silbert, L. E., Liu, A. J. & Nagel, S. R. Vibrations and diverging length scales near the unjamming transition. *Phys. Rev. Lett.* **95**, 098301 (2005).
- Wyart, M. Scaling of phononic transport with connectivity in amorphous solids. *Europhys. Lett.* **89**, 64001 (2010).
- DeGiuli, E., Laversanne-Finot, A., Düring, G., Lerner, E. & Wyart, M. Effects of coordination and pressure on sound attenuation, boson peak and elasticity in amorphous solids. *Soft Matter* **10**, 5628–5644 (2014).
- Lerner, E., DeGiuli, E., Düring, G. & Wyart, M. Breakdown of continuum elasticity in amorphous solids. *Soft Matter* **10**, 5085–5092 (2014).
- Wyart, M. Marginal stability constrains force and pair distributions at random close packing. *Phys. Rev. Lett.* **109**, 125502 (2012).
- Lerner, E., Düring, G. & Wyart, M. Low-energy non-linear excitations in sphere packings. *Soft Matter* **9**, 8252–8263 (2013).
- DeGiuli, E., Lerner, E., Brito, C. & Wyart, M. Force distribution affects vibrational properties in hard-sphere glasses. *Proc. Natl. Acad. Sci.* **111**, 17054–17059 (2014).
- Müller, M. & Wyart, M. Marginal stability in structural, spin, and electron glasses. *Annu. Rev. Condens. Matter Phys.* **6**, 177–200 (2015).
- Goodrich, C. P., Liu, A. J. & Sethna, J. P. Scaling ansatz for the jamming transition. *Proc. Natl. Acad. Sci.* **113**, 9745–9750 (2016).
- Baule, A., Morone, F., Herrmann, H. J. & Makse, H. A. Edwards statistical mechanics for jammed granular matter. *Rev. Mod. Phys.* **90**, 015006 (2018).
- Zaccone, A. & Scossa-Romano, E. Approximate analytical description of the nonaffine response of amorphous solids. *Phys. Rev. B* **83**, 184205 (2011).
- Pan, D., Meng, F. & Jin, Y. Shear hardening in frictionless amorphous solids near the jamming transition. *PNAS Nexus* **2**, pgad047 (2023).
- Hexner, D., Liu, A. J. & Nagel, S. R. Two diverging length scales in the structure of jammed packings. *Phys. Rev. Lett.* **121**, 115501 (2018).
- Hexner, D., Urbani, P. & Zamponi, F. Can a large packing be assembled from smaller ones? *Phys. Rev. Lett.* **123**, 068003 (2019).
- Charbonneau, P., Kurchan, J., Parisi, G., Urbani, P. & Zamponi, F. Fractal free energy landscapes in structural glasses. *Nat. Commun.* **5**, 3725 (2014).
- Charbonneau, P. et al. Numerical detection of the gardner transition in a mean-field glass former. *Phys. Rev. E* **92**, 012316 (2015).
- Berthier, L. et al. Growing timescales and lengthscales characterizing vibrations of amorphous solids. *Proc. Natl. Acad. Sci.* **113**, 8397–8401 (2016).
- Berthier, L. et al. Gardner physics in amorphous solids and beyond. *J. Chem. Phys.* **151**, 010901 (2019).
- Li, H., Jin, Y., Jiang, Y. & Chen, J. Z. Determining the nonequilibrium criticality of a gardner transition via a hybrid study of molecular simulations and machine learning. *Proc. Natl. Acad. Sci.* **118**, e2017392118 (2021).
- Urbani, P., Jin, Y. & Yoshino, H. The gardner glass. In: *Spin glass theory and far beyond: replica symmetry breaking after 40 years*, 219–238 (World Scientific, 2023).
- Charbonneau, P., Corwin, E. I., Parisi, G. & Zamponi, F. Jamming criticality revealed by removing localized buckling excitations. *Phys. Rev. Lett.* **114**, 125504 (2015).
- Wang, Y., Shang, J., Jin, Y. & Zhang, J. Experimental observations of marginal criticality in granular materials. *Proc. Natl. Acad. Sci.* **119**, e2204879119 (2022).
- Parisi, G., Pollack, Y. G., Procaccia, I., Rainone, C. & Singh, M. Robustness of mean field theory for hard sphere models. *Phys. Rev. E* **97**, 063003 (2018).
- Goodrich, C. P., Liu, A. J. & Nagel, S. R. Finite-size scaling at the jamming transition. *Phys. Rev. Lett.* **109**, 095704 (2012).
- Olsson, P. & Teitel, S. Critical scaling of shear viscosity at the jamming transition. *Phys. Rev. Lett.* **99**, 178001 (2007).
- Olsson, P. & Teitel, S. Critical scaling of shearing rheology at the jamming transition of soft-core frictionless disks. *Phys. Rev. E* **83**, 030302 (2011).
- Kawasaki, T., Coslovich, D., Ikeda, A. & Berthier, L. Diverging viscosity and soft granular rheology in non-brownian suspensions. *Phys. Rev. E* **91**, 012203 (2015).
- Heussinger, C. & Barrat, J.-L. Jamming transition as probed by quasistatic shear flow. *Phys. Rev. Lett.* **102**, 218303 (2009).
- Vagberg, D., Valdez-Balderas, D., Moore, M., Olsson, P. & Teitel, S. Finite-size scaling at the jamming transition: corrections to scaling and the correlation-length critical exponent. *Phys. Rev. E* **83**, 030303 (2011).
- Olsson, P. & Teitel, S. Dynamic length scales in athermal, shear-driven jamming of frictionless disks in two dimensions. *Phys. Rev. E* **102**, 042906 (2020).
- Vinutha, H., Ramola, K., Chakraborty, B. & Sastry, S. Timescale divergence at the shear jamming transition. *Granul. Matter* **22**, 16 (2020).
- Kumar, N. & Luding, S. Memory of jamming—multiscale models for soft and granular matter. *Granul. Matter* **18**, 58 (2016).
- Bertrand, T., Behringer, R. P., Chakraborty, B., O'Hern, C. S. & Shattuck, M. D. Protocol dependence of the jamming transition. *Phys. Rev. E* **93**, 012901 (2016).
- Baity-Jesi, M., Goodrich, C. P., Liu, A. J., Nagel, S. R. & Sethna, J. P. Emergent so (3) symmetry of the frictionless shear jamming transition. *J. Stat. Phys.* **167**, 735–748 (2017).
- Jin, Y. & Yoshino, H. A jamming plane of sphere packings. *Proc. Natl. Acad. Sci.* **118**, e2021794118 (2021).
- Chaudhuri, P., Berthier, L. & Sastry, S. Jamming transitions in amorphous packings of frictionless spheres occur over a

- continuous range of volume fractions. *Phys. Rev. Lett.* **104**, 165701 (2010).
49. Ozawa, M., Kuroiwa, T., Ikeda, A. & Miyazaki, K. Jamming transition and inherent structures of hard spheres and disks. *Phys. Rev. Lett.* **109**, 205701 (2012).
50. Ashwin, S., Blawdziewicz, J., O'Hern, C. S. & Shattuck, M. D. Calculations of the structure of basin volumes for mechanically stable packings. *Phys. Rev. E* **85**, 061307 (2012).
51. Martiniani, S., Schrenk, K. J., Ramola, K., Chakraborty, B. & Frenkel, D. Numerical test of the edwards conjecture shows that all packings are equally probable at jamming. *Nat. Phys.* **13**, 848–851 (2017).
52. Pine, D. J., Gollub, J. P., Brady, J. F. & Leshansky, A. M. Chaos and threshold for irreversibility in sheared suspensions. *Nature* **438**, 997–1000 (2005).
53. Corte, L., Chaikin, P. M., Gollub, J. P. & Pine, D. J. Random organization in periodically driven systems. *Nat. Phys.* **4**, 420–424 (2008).
54. Schreck, C. F., Hoy, R. S., Shattuck, M. D. & O'Hern, C. S. Particle-scale reversibility in athermal particulate media below jamming. *Phys. Rev. E* **88**, 052205 (2013).
55. Nagasawa, K., Miyazaki, K. & Kawasaki, T. Classification of the reversible–irreversible transitions in particle trajectories across the jamming transition point. *Soft Matter* **15**, 7557–7566 (2019).
56. Das, P., Vinutha, H. & Sastry, S. Unified phase diagram of reversible–irreversible, jamming, and yielding transitions in cyclically sheared soft-sphere packings. *Proc. Natl Acad. Sci.* **117**, 10203–10209 (2020).
57. O'Hern, C. S., Langer, S. A., Liu, A. J. & Nagel, S. R. Random packings of frictionless particles. *Phys. Rev. Lett.* **88**, 075507 (2002).
58. Binder, K. Finite size effects on phase transitions. *Ferroelectrics* **73**, 43–67 (1987).
59. Kawasaki, T. & Miyazaki, K. Unified understanding of nonlinear rheology near the jamming transition point. *Phys. Rev. Lett.* **132**, 268201 (2024).
60. Babu, V., Pan, D., Jin, Y., Chakraborty, B. & Sastry, S. Dilatancy, shear jamming, and a generalized jamming phase diagram of frictionless sphere packings. *Soft Matter* **17**, 3121–3127 (2021).
61. Xing, Y. et al. Origin of the critical state in sheared granular materials. *Nat. Phys.* **20**, 646–652 (2024).
62. Luding, S., Jiang, Y. & Liu, M. Un-jamming due to energetic instability: statics to dynamics. *Granul. Matter* **23**, 1–41 (2021).
63. Behringer, R. P., Bi, D., Chakraborty, B., Henkes, S. & Hartley, R. R. Why do granular materials stiffen with shear rate? test of novel stress-based statistics. *Phys. Rev. Lett.* **101**, 268301 (2008).
64. Boschan, J., Luding, S. & Tighe, B. P. Jamming and irreversibility. *Granul. matter* **21**, 1–7 (2019).
65. Seto, R., Singh, A., Chakraborty, B., Denn, M. M. & Morris, J. F. Shear jamming and fragility in dense suspensions. *Granul. Matter* **21**, 1–8 (2019).
66. Bi, D., Zhang, J., Chakraborty, B. & Behringer, R. P. Jamming by shear. *Nature* **480**, 355–358 (2011).
67. Zhao, Y. et al. Shear-jammed, fragile, and steady states in homogeneously strained granular materials. *Phys. Rev. Lett.* **123**, 158001 (2019).
68. Binder, K. Theory of first-order phase transitions. *Rep. Prog. Phys.* **50**, 783 (1987).
69. Kierlik, E., Monson, P., Rosinberg, M. & Tarjus, G. Adsorption hysteresis and capillary condensation in disordered porous solids: a density functional study. *J. Phys. Condens. Matter* **14**, 9295 (2002).
70. Nattermann, T. Theory of the random field Ising model. In: *Spin glasses and random fields*, 277–298 (World Scientific, 1998).
71. Rossi, S. Effective theory of the yielding transition in amorphous solids. Ph.D. thesis, Sorbonne Université (2023).
72. Ozawa, M., Berthier, L., Biroli, G., Rosso, A. & Tarjus, G. Random critical point separates brittle and ductile yielding transitions in amorphous materials. *Proc. Natl. Acad. Sci.* **115**, 6656–6661 (2018).
73. Zhang, K., Li, X., Jin, Y. & Jiang, Y. Machine learning glass caging order parameters with an artificial nested neural network. *Soft Matter* **18**, 6270–6277 (2022).
74. Knight, J. B., Fandrich, C. G., Lau, C. N., Jaeger, H. M. & Nagel, S. R. Density relaxation in a vibrated granular material. *Phys. Rev. E* **51**, 3957 (1995).
75. Ikeda, H. Control parameter dependence of fluctuations near jamming. *J. Chem. Phys.* **158**, 056101 (2023).
76. Bi, D., Henkes, S., Daniels, K. E. & Chakraborty, B. The statistical physics of athermal materials. *Annu. Rev. Condens. Matter Phys.* **6**, 63–83 (2015).
77. Pöschel, T. & Luding, S. *Granular gases*, vol. 564 (Springer Science & Business Media, 2001).
78. Yao, L. & Jack, R. L. Thermal vestiges of avalanches in the driven random field Ising model. *J. Stat. Mech. Theory Exp.* **2023**, 023303 (2023).
79. Song, C., Wang, P. & Makse, H. A. A phase diagram for jammed matter. *Nature* **453**, 629–632 (2008).
80. Ramaswamy, M. et al. Universal scaling of shear thickening transitions. *J. Rheol.* **67**, 1189–1197 (2023).
81. Lees, A. & Edwards, S. The computer study of transport processes under extreme conditions. *J. Phys. C: Solid State Phys.* **5**, 1921 (1972).
82. Bitzek, E., Koskinen, P., Gähler, F., Moseler, M. & Gumbsch, P. Structural relaxation made simple. *Phys. Rev. Lett.* **97**, 170201 (2006).

Acknowledgements

We warmly thank Hajime Yoshino, Stephen Teitel, Bulbul Chakraborty, Olivier Dauchot, Gilles Tarjus, and Yujie Wang for inspiring discussions. We acknowledge financial support from NSFC (Grants 12161141007, 11935002, 11974361, and 12047503), from Chinese Academy of Sciences (Grants ZDBS-LY-7017 and KGFZD-145-22-13), and from Wenzhou Institute (Grant WIUCASQD2023009). In this work, access was granted to the High-Performance Computing Cluster of the Institute of Theoretical Physics - the Chinese Academy of Sciences.

Author contributions

Y.D., D.P., and Y.J. contributed equally to this work.

Competing interests

The authors declare no competing interests.

Additional information

Supplementary information The online version contains supplementary material available at <https://doi.org/10.1038/s41467-024-51319-4>.

Correspondence and requests for materials should be addressed to Yuliang Jin.

Peer review information *Nature Communications* thanks Adrian Baule, and the other, anonymous, reviewer for their contribution to the peer review of this work. A peer review file is available.

Reprints and permissions information is available at <http://www.nature.com/reprints>

Publisher's note Springer Nature remains neutral with regard to jurisdictional claims in published maps and institutional affiliations.

Open Access This article is licensed under a Creative Commons Attribution-NonCommercial-NoDerivatives 4.0 International License, which permits any non-commercial use, sharing, distribution and reproduction in any medium or format, as long as you give appropriate credit to the original author(s) and the source, provide a link to the Creative Commons licence, and indicate if you modified the licensed material. You do not have permission under this licence to share adapted material derived from this article or parts of it. The images or other third party material in this article are included in the article's Creative Commons licence, unless indicated otherwise in a credit line to the material. If material is not included in the article's Creative Commons licence and your intended use is not permitted by statutory regulation or exceeds the permitted use, you will need to obtain permission directly from the copyright holder. To view a copy of this licence, visit <http://creativecommons.org/licenses/by-nc-nd/4.0/>.

© The Author(s) 2024